Fine sediment dynamics over a gravel bar. Part 1: Validation of a new image-based segmentation method

Junjian Deng, Thomas Drevet, Lionel Pénard, Benoît Camenen

Version of Record: https://www.sciencedirect.com/science/article/pii/S0341816223000693
Manuscript_aefa6b98074e4be9ecb9b144adfa83c4

Fine sediment dynamics over a gravel bar. Part 1: Validation of a new image-based segmentation method

Junjian Deng[a], Thomas Drevet[a], Lionel Pénard[a], Benoît Camenen[a,*]

[a]*Inrae, UR RiverLy, centre de Lyon-Grenoble, Villeurbanne, France*

Abstract

In this paper, we present a new image processing algorithm to analyse fine sediment deposits on gravel bars. The method is based on pictures taken from the river bank with an average resolution of a few centimetres per pixel. The proposed image processing algorithm consists of two steps. In the first step, the raw image is orthorectified with a 5 cm pixel size. In second step, we used an original combination of two well-known image techniques to classify pixel. First, a high-pass filter is applied in the Fourier domain to correct grey-value potential bias, i.e. to merge wet and dry deposits. Then, an unsupervised classification process based on K-means clustering is conducted to partition image pixels into K classes. The area of fine sediment deposits is calculated by summing the area of each class multiplied by weighting parameters (surface area percentage of fine deposits for each class). The value of K and the weighting parameters are calibrated using local close range photos of the bar surface representing the spatial variation of surface fine sediment distribution. The algorithm is then validated with field measurement using the finest class ($d < 4$ mm) of Wolman pebble count method. The impact of image resolution is investigated: the algorithm was found suitable for pixel size between 1 and 10 cm. The robustness of the present algorithm to images taken at different times and with different illuminations is studied by comparing it to two methods from the literature. The new method yields the most robust results with an average standard deviation lower than 5%. It yields larger surface of fine sediment since it includes all possible patches around coarse particles. Such results imply that the algorithm can be applied on a long image series to help us understand the temporal dynamics of fine sediment deposits on the bar surface.

Keywords: Fine sediment deposit, Image-based segmentation, Remote sensing, Alpine rivers, Gravel bar

*Corresponding author, benoit.camenen@inrae.fr

1. Introduction

Alpine rivers are usually characterised by a large amount of fine sediments travelling over the gravel-bed system as suspension (Lenzi et al., 2003; Navratil et al., 2010; Camenen et al., 2016; Pagano et al., 2019; Misset et al., 2019; Antoine et al., 2020). These suspended sediment loads are associated with important socio-economic (flooding, damage to infrastructure, ...) and environmental (ecological habitats, nutrient transport, ...) issues (Vercruysse et al., 2017; Juez et al., 2018). High suspended sediment concentrations during flood events usually lead to large deposits on gravel bars (Kondolf and Wilcock, 1996). Wohl and Cenderelli (2000); Rathburn and Wohl (2003) showed that fine sediment deposition occurs primarily in pools and in lateral eddies. In addition, flood event duration and flow velocity govern the volume and grain size distribution of this deposition (Camenen et al., 2016). Such deposits impact the sedimentary construction of the river and may lead to stratifications (Wang et al., 2008). Furthermore, changes in channel morphology and large deposits of fine sediments may also have an impact on the vegetation dynamics in the river channel (Jourdain et al., 2020) and on fish habitat due to clogging of interstices as observed by Lisle (1989); Kondolf and Wilcock (1996); Wood and Armitage (1997); Liu et al. (2004). The development of gravel bars and pools is essential for spawning habitat for fishes, and for rheophilic invertebrate species but their habitat conditions remain very sensitive to the grain size distribution (Rubin et al., 2004; Kemp et al., 2011). In a flood-regulated river, Grams and Schmidt (2002) showed that the aggradation of the downstream reach was accompanied with fine sediment accumulation along riverbanks and gravel bars in the absence of high intensity flows. Folk and Ward (1957); Konrad et al. (2002); Cordier et al. (2020) also showed that gravel bars had a significant importance in grain sorting and sediment transfer along the river. Thus, there is a need to better understand the fine sediment deposit characteristics and dynamics as a continuously varying patchy environment (Fausch et al., 2002).

Suspended sediment load can be continuously and remotely measured in a river by combining the turbidity-water discharge measurements. However the surface fine sediment deposition and fine sediment stocks in the river system can only be evaluated occasionally and locally by collecting samples in the field (Lambert and Walling, 1988; Navratil et al., 2010; Piqué et al., 2014; Misset et al., 2021). Moreover, field experiments, which consist in evaluating the grain size distribution of a surface patch, is extremely time-consuming (sampling, sieving, sediment drying, etc.). So the investigation

of fine sediment dynamics is thus limited in the temporal and spatial scale. One solution could be to use a numerical hydro-sedimentary model calibrated with discrete local measurement to generate deposition data. Such models remain however difficult to validate and to apply to large domains.

Several investigations highlighted the possibility of using image processing analysis to directly estimate the grain size distribution in an orthorectified image. These methods can be simply divided into two categories: (i) delineation methods (Graham et al., 2005; Detert and Weitbrecht, 2012; Carbonneau et al., 2018; Purinton and Bookhagen, 2019), which allow the full delineation and measurement of every visible grain in the image, and (ii) texture methods (Carbonneau et al., 2004; Verdú et al., 2005; Buscombe, 2013; Black et al., 2014; Buscombe, 2020; Lang et al., 2020), which use the statistical analysis of image intensity and texture to extract grain-size information from digital imagery. The benefits of delineation methods are that segmentation does not require any site calibration but only knowledge of the image scale in order to estimate a full detailed grain size distribution. Among these methods, a free application called *Basegrain* developed by Detert and Weitbrecht (2012) has become a reference tool. It is based on edge detection followed by watershed segmentation (a classical image segmentation algorithm) and ellipse fitting. It is worth noting that delineation methods often require high spatial resolution point clouds and/or close-range images, which limited these methods to small areas. Furthermore, these methods could not delineate particles smaller than a few pixels, which is often the case for fine sediments. In contrast, texture methods could be used to evaluate the grain size distribution for a large surface area and different image resolutions. Carbonneau et al. (2004) and Verdú et al. (2005) worked on a small subset of grey-level co-occurrence matrix parameters on the image texture to possibly map the grain size distribution down to sand-size particles. In the recent years, researches showed that machine learning techniques performed well for image classification and regression, specifically the convolutional neural network (CNN) as a type of artificial neural network (ANN). Buscombe (2020) used CNNs to develop a data-driven machine-learning framework called SediNet to predict the grain size distribution as well as sediment population and sediment shapes. Lang et al. (2020) also developed a CNN model called GRAINet to provide an end-to-end estimation of the grain size distribution. These two models could both predict the grain size distribution without knowing the image scale. Despite the fact that most of these methods could remotely measure the grain size distribution in either a close range image or a high airborne image, few studies focused on the fine sediment mapping. However, fine sediments are extremely dynamic and their surface distribution over gravel bars can vary significantly during a year (Came-

nen et al., 2013). Camenen et al. (2013) thus developed a method based on the shape of the local image histogram to determine thresholds between fine, mixed and coarse sediments and then segment the image into different classes of sediment over the bar surface. This method is easy to implement, but threshold values need to be changed when acquisition conditions vary (sun/clouds, time of the day, shadows, season, etc.). So when dealing with a large amount of image data, the calibration of the histogram thresholds for each image would be time-consuming and inefficient. Carbonneau et al. (2005) also proposed a texture-based image segmentation method to quantify the superficial sand presence in dry exposed fluvial gravel bars. The method is based on the textural contrast calculation following a 3×3 pixel-size windowed application of the co-occurrence matrix. The acquired textural image was then segmented into two classes (sand and clasts) using the method of Otsu (1979). This method is also easy to implement and efficient, however the authors mentioned the limitation of the method dealing with silts and clay. Moreover, the method was only applied to the images of dry sand sediments, the application of this method in a mixed moisture situation where the fine sediments were partially dry and wet still remains unclear. Given that the fine sediments close to the main channel and secondary channels were often wet and those on the high elevation bar surface were dry, a robust image segmentation method allowing to deal with varying moisture condition of the fine sediments is required.

Over the last decades, unsupervised clustering procedures were largely built up to segment images into different meaningful clusters for further investigation. In general, clustering methods allow to separate image pixels into different clusters where pixels inside one cluster should be similar according to some metric (e.g. intensity), while different from pixels from other clusters (Jain et al., 1999; Nelson et al., 2014). Several types of clustering algorithms are used in image segmentation, such as partitional clustering, hierarchical clustering, and density based clustering. Among these clustering algorithms, the K-means clustering algorithm (a partitional clustering) is the most popular algorithm because of its simplicity and efficiency compared to other clustering algorithms, even though a priori knowledge of the numbers of the clusters is needed (MacQueen et al., 1967; Jain and Dubes, 1988). This technique thus shows a potential application to the fluvial sedimentary images for the bed surface sedimentary investigation (Nelson et al., 2014). Nevertheless, to our best knowledge, no study was made so far to segment images for the fine sediment investigation using K-means type clustering methods.

With the objective of improving the understanding of fine sediment deposits on the gravel bar surface using image processing method, we propose

a new method to delineate fine sediment deposits over a gravel bar. To overcome the limitations of previous studies (Carbonneau et al., 2005; Camenen et al., 2013), this method is based on the application of a high-pass filter so that it is more robust to the low-frequency moisture variation of the fine sediments and to illumination changes. This step is followed by the K-means clustering algorithm. The method uses an orthorectified photo taken by a time-lapse camera from the river bank to automatically classify fine sediment pixels. The camera system is cheap, easy to set-up and allows to acquire images with a frequency of a few images per day. The method is designed to be robust and efficient, so it can be used to process automatically a long time series of photos to investigate temporal variation of fine sediment dynamics on a gravel bar surface. A calibration of the method is conducted using local close range photos of the bar surface from different positions to represent the spatial variation of surface fine sediment distribution. Using the optimised parameters found in the calibration step, we then validated the algorithm with field measurement using the Wolman pebble count method. A discussion on the robustness of the method and related uncertainties is also provided.

2. Methodology

2.1. Study site

Experiments were made on the River Arc in the French Alps (Figure 1). The River Arc bed is a typical engineered European alpine river, straightened, embanked and used for hydroelectricity production. It is characterised by systems of alternate bars. A significant amount of fine sediment deposits are constantly observed on gravel bars along the river over time (Camenen et al., 2016). Most of the fine sediment flux occurs during the snow melt season (May to July), the fine sediments mainly coming from the highly erodible sub-catchments. Antoine et al. (2020) showed that short term hydrological events such as dam flushing events and floods can also transport a large amount of fine sediments, and stocks from the deposits on the bars' surface, which are non-negligible in the fine sediment budget.

The area of interest is located on a 250 m long gravel bar, part of an alternate bar system (Jaballah et al., 2015), located on the left bank side of the river, approximately 16 km downstream Saint-Martin-la-Porte reservoir (Figure 1). Lateral limits are set by 5 m high embankments made of boulders and scattered trees. The mean slope of this reach is approximately 0.6%. Over this reach, the grain size distribution is poorly sorted and typical median grain size diameter varies from 10 cm on the bar head to 2 cm on the bar tail (Jodeau, 2007). Fine sediment deposits observed on the gravel bar are

composed of a sand and silt mixture (Camenen et al., 2016), made of black marlstone.

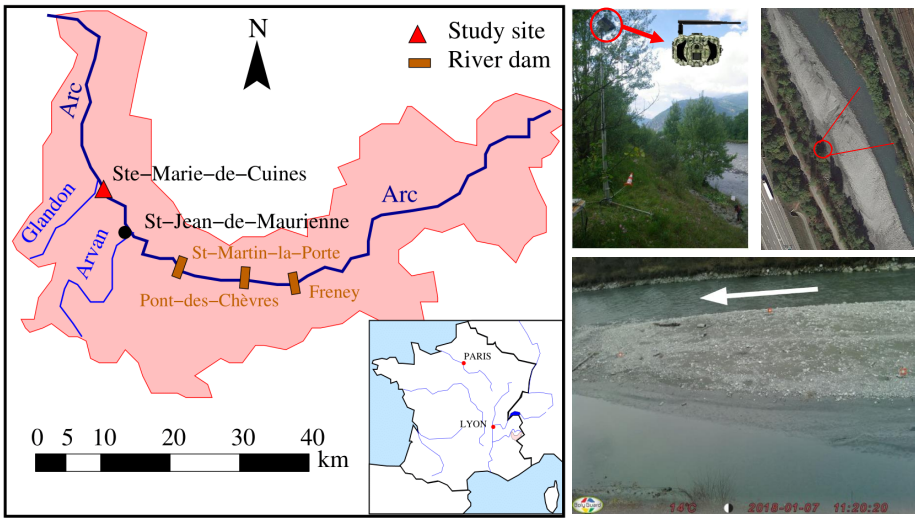

Figure 1: Left: Study site location at Ste-Marie-de-Cuines (the red triangle indicates the location of the studied gravel bar in the Arc river) and right: a view of the camera setup, a top view of entire bar and an example of the image took from the camera (white arrow indicates the flow direction).

2.2. Data collection

2.2.1. Image acquisition system

A commercial digital trail camera (Bolyguard MG983G-30M) was installed in May 2017 on the top of the left bank, attached to a tree trunk in order to monitor the bar surface with the most favourable viewing angle. The image sensor corresponds to a 14MP colour CMOS with 20MP and 30MP interpolation. The focal length is 7.4 ± 5% mm, the camera field of view is 57°, and the optical distortion is less than -1 % (barrel distortion). Approximately one third of the gravel bar lays within the camera field of view. Due to the location of the camera, a shooting angle of around 60° is introduced in each image. The camera is set on the Time Lapse mode to allow to capture 30MP images with a ground resolution varying from 2 to 5 centimetres on the bar surface, depending on the distance to the camera. The camera was set to take two images per day, one in the morning and one in the afternoon. A two-year image series was thus acquired from 2018 to 2020.

2.2.2. Image subset for investigation of robustness to weather condition

Among our two-year image series, variation of image quality was observed due to different weather conditions. To investigate the impact of weather conditions on the image quality, a set of 55 images was selected. These images were taken during the dry season in February 2018, for which discharge was consistently around 6 m^3/s. No significant hydrological and hydro-climatic event took place during this period; it can thus be assumed that the fine deposit surface area is constant during this period. Table 1 summarizes four major weather conditions that appeared in this subset. On the first line of Table 1, the image corresponds to a specific case when a valley fog took place. The view of gravel bar is blurry and the texture of sediment becomes unclear. The second example was taken in a morning when there was a clear sky in the valley. The third image was taken on the same day as the first one but in the afternoon, which was sunny. The sun in the afternoon makes a few long inclined tree shadows on the bar, which makes the deposit zone fuzzier. Coarse sediments can be clearly observed and the texture of different types of sediment is distinguishable. The last one was taken on a cloudy morning. Compared to Image 3, the bar surface is more homogeneous because of the less powerful sun light on the surface; a lower contrast appears between coarse and fine sediments, however, the deposit zone is still distinguishable.

Weather condition	Number of Images	Example image	Image quality
Foggy	3		Degraded due to the fog
Sunny morning	10		High contrast and clear texture
Sunny afternoon	12		Trunk shadow on the bar's surface, high contrast, and clear texture
Cloudy	30		Low contrast and low texture

Table 1: Summary of image quality depending on the weather condition in the image subset.

2.2.3. Complementary bed surface data

Drone images taken on 12 July 2017 are also available on the studied site. They were taken vertically, with a ground resolution of 1 cm. We subsampled these images to obtain several resolutions: 1 cm, 3 cm, 5 cm, 10 cm, 15 cm and 20 cm. These images were used to assess the applicability of our method on images with different resolutions.

In addition, we also took 11 local close range images in January 2019 at different locations on the bar surface, chosen to take into account a large variety of sediment distributions and surface textures (Figure 2). We used a Sony HX99 compact camera model (18 MP image, focal length of 4.2 mm). The image ground resolution is 0.5 mm/px. Every image was taken vertically to ensure that no shooting angle is introduced, and every image was georeferenced using DGPS. These close range images were used to get highly

detailed ground truth data about the two sediment classes, fine and coarse, in order to calibrate the method.

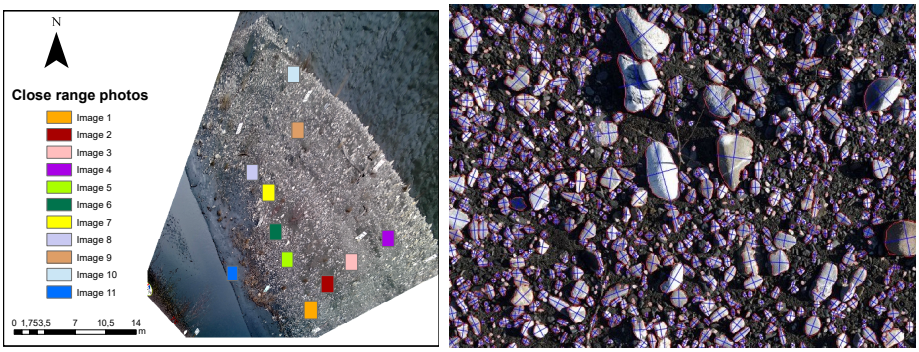

Figure 2: Left: Location of 11 close range photos on the studied gravel bar, and right: Manually corrected output from *Basegrain* for Image 1 within the 11 close range photo data (see Section 2.3.1).

Finally, several evaluations of the surface grain size distribution at different locations over the gravel bar were made in June 2019 just before and after a dam flushing event using the Wolman (1954) pebble count method. The studied patches were chosen to be representative of the bar surface diversity and their location is displayed in Figure 3. In each patch, we collected around 200 grains along several back and forth transects and we measured each particle's b-axis. The grain size distribution curve of all Wolman samples is plotted in Figure 3. They were used as ground truth data to assess the validity of our method's results.

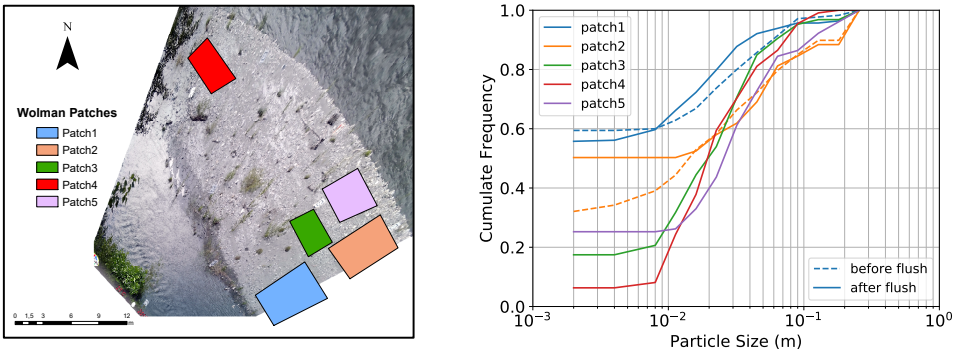

Figure 3: Left: Location of the Wolman pebble count method's patches, and right: grain size distribution curves from the Wolman pebble count method.

2.3. Ground truth data generation

2.3.1. Areal ratio of fine sediment deposits using close range photos

We constructed our ground truth data using the close range photos taken on the bar surface. At first, the grains in each photo were automatically detected by using *Basegrain* (Detert and Weitbrecht, 2012) (reference tool in the literature for the grain size distribution analysis in a close range image). The minimum grain area detected by *Basegrain* was around 10 pixels, which corresponded to a minimum grain size of 5 mm. Then, we corrected each output of *Basegrain* manually to minimize the errors from the automatic detection (e.g. missing detection, grain overlap, over-detection, etc.). An example of the output of *Basegrain* is presented in Figure 2 (all results are given in the Supplementary Material). It is worth noting that *Basegrain* was designed to estimate the coarse particles; so, in order to be comparable with our proposed method, we assumed that the undetected area from the *Basegrain* result was the fine sediment area (with grain size lower than 5 mm). Under this assumption, the fine sediment areal ratio $\Phi^f_{S,Base}$ for each image was then calculated as follows:

$$\Phi^f_{S,Base} = 1 - \frac{S_d}{S_j}, \tag{1}$$

where S_d is the detected area in the close range image of total area S_j of the image. The 11 fine sediment areal ratios were thus obtained and formed the ground truth data used to calibrate our method.

2.3.2. Conversion from volumetric to areal sampling for the Wolman data

The Wolman pebble count method provided an evaluation of the volumetric ratio ($\Phi^i_{V,Wol}$) whereas the image processing method provided an areal ratio. Therefore, to be able to compare the results of these two methods, we need to convert the Wolman data to an areal grain size distribution. Using the American template FISP US SAH97 to measure the collected samples, the minimum grain size that we measured was 4 mm. We tallied all particles smaller than 4 mm in the $d < 4$ m class as Bunte and Abt (2001) suggested. Therefore, we used the $d < 4$ mm frequency in the grain size distribution from the Wolman method to represent the fine sediment frequency. This analysis of the samples was conducted for all five patches.

The Wolman grain size distribution was transformed into the areal grain size distribution $\Phi^i_{S,Wol}$ by the following equation suggested by Bunte and Abt (2001):

$$\Phi^i_{S,Wol} = \frac{S^i_{Wol}}{\Sigma^n_{j=1} S^j_{Wol}} = \frac{\Phi^i_{V,Wol} \times 1\ \mathrm{m}^3}{D^i_{Wol} \Sigma^n_{j=1} S^j_{Wol}} \tag{2}$$

where D^i_{Wol} is the diameter of class i; $S^i_{Wol} = (\Phi^i_{V,Wol} \times 1\ \mathrm{m}^3)/D_i$ is the equivalent area for class i with the term 1 m^3 being added for units correspondence; n is the number of sediment classes.

The statistical error for Wolman measurements is estimated according to Bunte and Abt (2001), that is a function of the percentile of the fine sediment class; the reader may refer to the Supplementary Material for details.

2.4. Image processing methodology

2.4.1. Preprocessing steps

The proposed method does not work directly on raw images acquired from the trail camera, it requires several preprocessing steps: (1) internal camera calibration (done only once); (2) camera position and exterior orientation estimation, with ground reference points (GRPs); (3) orthorectification to obtain equally sized pixels throughout the image and remove distortions so that we can display both image and segmentation results in a GIS software. The orthorectification step requires knowledge of camera intrinsic and extrinsic parameters along with a Digital Elevation Model (DEM) of the area. Camera calibration was performed using the OpenCV image processing library in Python (Bradski, 2000) to get the intrinsic parameters (focal length, optical centre projection, distortion). Similarly, the extrinsic parameters (location and orientation of the camera) were computed by matching between the GRPs in the field 3D coordinates and them in the image 2D coordinates. To do so, we implemented a set of GRP targets on the bar surface in the camera field of view to specify the position of the GRPs. The 3D real-world coordinates of the GRPs were acquired by measuring directly the coordinates of these targets using DGPS (positioning errors ranged from 1.7 to 3.4 centimetres). The pixel coordinates of the GRPs were obtained manually from the input bank-view images. The translation and the rotation vectors were then estimated using measured 3D coordinates and pixel coordinates of GRPs. The extrinsic parameters are thus estimated based on these two vectors using OpenCV build-in functions. Once knowing the camera position and orientation, the final orthorectification is conducted to project image pixels into 3D coordinates.

Several topographic surveys were carried out to produce the DEMs (called measured DEMs) used during the orthorectification step. The gravel bar was found to be nearly flat and horizontal, so a flat DEM was also considered to produce the orthoimages, and the results of the method are given using it. The comparison between measured and flat DEMs is discussed in section 3.3. The orthorectified image resolution is 5 cm in accordance with the initial image resolution.

2.4.2. Classification

The classification is based on the following general observations: (1) For each single image, fine sediments generally result in a lower image brightness than coarse sediments because of their different texture. This difference of texture can be distinguished in the frequency domain as the fine sediments have a longer period and lower magnitude frequency. Also, the edge of the coarse sediments is often easy to recognise in the image because of the abrupt change of intensity. This local variation of intensity is presented by a shorter period and higher magnitude frequency in the frequency domain. Therefore, a filter in the frequency domain can be applied to enhance the intensity difference between the fine sediments and coarse sediments for an easier classification; (2) In addition, the low frequency also corresponds to the slow spatial intensity change of fine sediments due to the change of moisture or the variation of brightness. This property is useful for classification when dealing with the different wetness conditions of fine sediment present at the same time in the image. In our image data, we often found that either all the fine sediments are wet (after a rain event or a total submersion due to the flood event), or the centre of the bar is dry whereas a strip of wet fine sediments is present on the edge of the bar, in particular along the secondary channel (in most of cases).

Based on these general observations, our motivations were at first to suppress low frequency trends in the intensity variations, then to apply a robust segmentation. To realise these motivations, our method includes two main steps. In the first step a high-pass filter (HPF) is applied to the image in the frequency domain to suppress low frequencies. This technique is commonly used in the image processing; we use it to enhance the intensity of the coarse sediments to be more distinguishable and to remove the moisture and brightness variations of fine sediments. In the second step, pixels are classified into different clusters based on their filtered intensity using K-means clustering. Figure 4 gives an overview of classification steps.

Step 1: High-Pass Filter

We firstly convert the input RGB image into a greyscale image. Next, we transform the image signal into the frequency domain using a 2D fast-Fourier transform (FFT). In the frequency domain, we apply a square HPF, consisting in setting to zero the low frequency values inside a $\omega \times \omega$ square window at the centre of the frequency domain. Finally the image is transformed back to the greyscale spatial domain by doing an inverse FFT. The converted image is then ready for the next step. The size ω of the HPF is determined after a sensitivity analysis. This ω value is investigated from 1 to image width. Results are found to be not sensitive to ω if $\omega \in [5; \text{image width}]$. In this

study, we set $\omega = 150$.

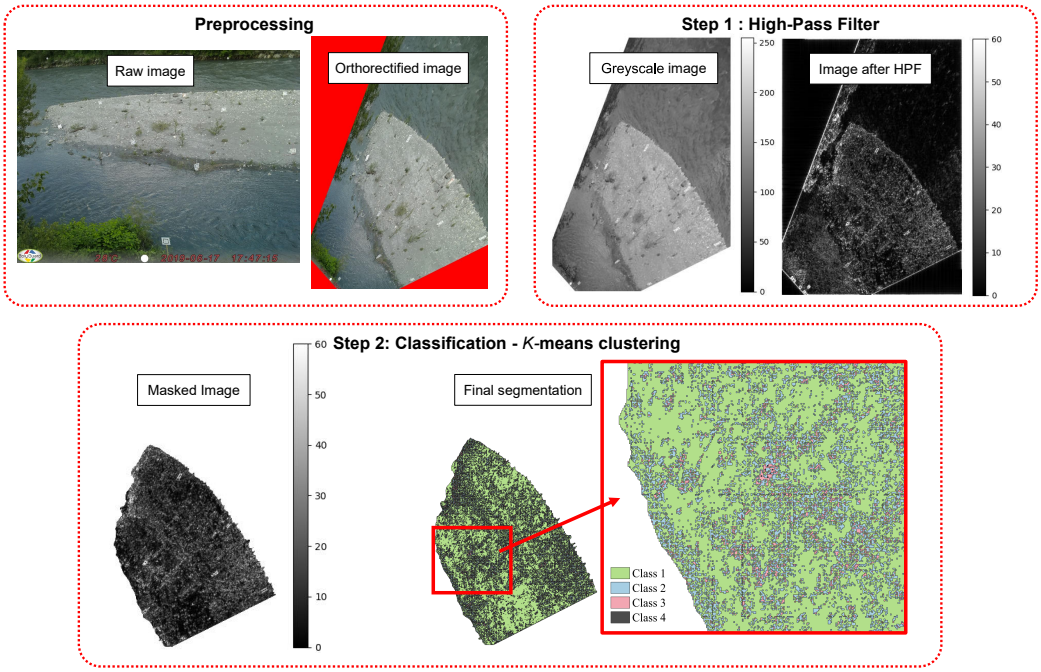

Figure 4: Schematic view of image processing method. Preprocessing: A raw image acquired by the camera system is orthorectified with a resolution of 5 cm. Step 1: A HPF is used to cutoff the low frequency to highlight the textural elements. Step 2: Image is masked to remove all the elements that are not part of the gravel bar (water, vegetation etc.) and segmented based on the value of pixels using K-means clustering.

Step 2: Classification - K-means clustering

A 1D K-means clustering algorithm coded in a OpenCV function is used to segment the image after HPF, into K classes with respect to the value of the pixels. Pixels with lower values represent fine sediments as they have little or no texture. On the contrary, the pixels containing gravel / pebbles have higher values as they can be identified easily because of a high texture. The K-means algorithm thus finds the optimal thresholds between K classes and classifies the pixels into K classes from lower value to higher value according to these thresholds (c.f. right graph of Step 1 in Figure 4). Specifically, the K-means algorithm starts with randomly choosing K centroids, then the pixels closest to the centroids are grouped together. After grouping the pixels, the positions of K centroids are re-shifted to new positions estimated from the grouped pixels, then pixels are regrouped again according to these new centroids. The algorithm is iteratively executed and stops when the difference between the positions of the last iteration centroids and the positions of the

current centroids is under a threshold. In our case, this threshold is set to 0.1. The final result image is stored into a 2D array where pixels are labelled by the cluster number. We extract each class and binarize it for visualization. The area of each class S_K^i is then calculated.

Finally, we add a weighting parameter to each class to account for the area of fine sediments it contains. The final fine sediment areal ratio Φ_S^f for one K value thus read:

$$\Phi_{S,K}^f = \frac{\Sigma_{i=1}^K \alpha_K^i S_K^i}{S_j}, \tag{3}$$

where α_K^i is the weighting parameter and S_K^i is the area of class i (i =1, 2, ..., K).

A calibration is necessary to determine these weighting parameters, and is described in the next paragraph.

2.5. Calibration of the weighting parameters

The calibration objective is to find the most appropriate number of clusters K and the set of weighting parameters to have an optimized $\Phi_{S,K}^f$ that fits the ground truth data $\Phi_{S,Base}^f$. Two criteria are used to perform the calibration fit:

- the bias of average fine sediment areal ratio:

$$B_{\Phi_{S,K}^f} = \frac{1}{n}\Sigma_{j=1}^n(\Phi_{S,K}^f - \Phi_{S,Base}^f) \tag{4}$$

- the Root Mean Square Error (E_{RMS}):

$$E_{RMS} = \sqrt{\frac{1}{n}\Sigma_{j=1}^n(\Phi_{S,K}^f - \Phi_{S,Base}^f)^2} \tag{5}$$

with $n = 11$ the number of images. The optimised results are those who have the minimum bias and E_{RMS}.

Four different K values (K = 3, 4, 5, 6) are tested. For each K value, the weighting parameter for each class is evaluated by sweeping the parameter space with a step of 0.1

The calibration of the new method is conducted using the ground truth data generated from the close range photos presented in Section 2.3.1. To be consistent with the date of these close range photos, we select the most temporally close bank-view photo and apply the proposed method to it. The calibration is performed only once. Afterwards, these obtained optimised parameters are used for all the images.

2.6. Optional step: median filter

Results from the classification could produce isolated pixels for each class, or individual holes. To prevent this, another processing step could be added to the process: a median filter. It aims at removing isolated pixels and narrow lines of pixels from the results. The filter size is set to 5×5 pixels and it is applied to each class resulting from the K-means clustering. The weighting parameters are unchanged. This step is optional.

2.7. Robustness assessment

In order to assess the robustness of the method to illumination changes, weather condition and image quality, we investigate their effect by applying the calibrated method to the 55 images introduced in Table 1.

We compare the dependence of our method's results on weather condition to two methods from the literature. One is the method of Camenen et al. (2013) (hereinafter referred to as method of Camenen) written in Matlab and the other is an image analysis inspired by the method of Carbonneau et al. (2005) using the commercial software ENVI 5.3 (hereinafter referred to as method of Carbonneau). We apply the method of Camenen to the subset images using their proposed threshold values to distinguish different classes. Four classes are defined to segment the gravel bar surface according to the different histograms: fine deposit surface S^{f}_{Cam}, fine and coarse mixture surface S^{fc}_{Cam}, coarse and fine mixture surface S^{cf}_{Cam}, and coarse sediments surface S^{c}_{Cam}. The fine sediment areal ratio $\Phi^{f}_{S,Cam}$ is thus set as follows:

$$\Phi^{f}_{S,Cam} = \frac{S^{f}_{Cam}}{S^{f}_{Cam} + S^{fc}_{Cam} + S^{cf}_{Cam} + S^{c}_{Cam}}. \tag{6}$$

In terms of the method of Carbonneau, we use the supervised classification module and the co-occurrence filter in ENVI 5.3 software to detect the fine sediments. Following the description given in Camenen et al. (2013), the image pixels are at first classified into 4 classes (tag, wood, pebble and fine sediment) according to the spectral analysis using predefined training data. In parallel, the contrast value of each pixel is calculated from the co-occurrence matrix by applying a 3×3 pixels window approach over the entire image pixels. A threshold binarization is then conducted on the result of the co-occurrence filter to classify image pixels into 2 classes (homogeneous zone and non-homogeneous zone) according to the contrast value of the pixels. Finally, the pixels, classified both in the fine sediment class of the spectral analysis result and in the homogeneous zone class of the texture result, are selected as the final result to represent the fine sediment deposits. The fine sediment areal ratio is then calculated by dividing the selected area by the total studied area.

3. Results and discussions

3.1. Calibration using the close range photos

The optimised results for each K are plotted in Figure 5. The details of calibration for each K are presented in Table 2. According to the calibration results, the method is not sensitive to the value of K as all four different K value groups yield similar results. Moreover, the spatial distribution of fine sediment seems to be successfully reproduced by the new method as the difference between the new method fine sediment areal ratio and ground truth fine sediment areal ratio for different images is below 10%. The best result is obtained with $[\alpha_4^1, \alpha_4^2, \alpha_4^3, \alpha_4^4] = [1.0, 0.5, 0.1, 0.0]$ for $K = 4$, which represented 100% of Class 1, 50% of Class 2, 10% of Class 3, and 0% of Class 4. The minimum bias and E_{RMS} are +0.2% and 4.6%, respectively.

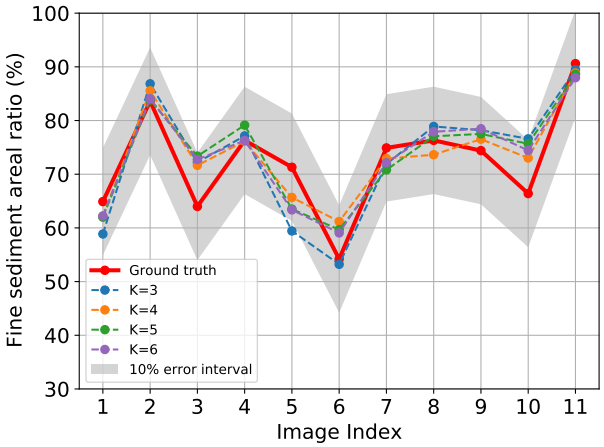

Figure 5: Comparison between ground true fine sediment areal ratio $\Phi^f_{S,Base}$ (red line) and the optimised image processing methodology areal ratio $\Phi^f_{S,K}$ (dashed line) for K = 3, 4, 5, 6.

	α_K^1	α_K^2	α_K^3	α_K^4	α_K^5	α_K^6	$B_{\Phi^f_{S,K}}$	E_{RMS}
$K = 3$	1.0	0	0	-	-	-	0.5%	6.0%
$K = 4$	1.0	0.5	0.1	0	-	-	0.9%	4.4%
$K = 5$	1.0	0.6	0.2	0.1	0	-	1.3%	5.3%
$K = 6$	1.0	0.8	0.3	0.1	0	0	1.1%	4.9%

Table 2: Optimized values of α_K^i after calibration with ground truth data.

However, the calibrated value of K and weighting parameters may no longer be suitable in an extreme case where there is 0% or 100% of fine sediment coverage in the whole image. This is due to the fact that the algorithm

imposes to segment image pixels into K classes and only 50%, 10% and 0% of pixels in Classes 2, 3 and 4 are taken into account as fine sediment according to the current calibration result. In these cases, the method would overestimate or underestimate the fine sediment area, respectively. The calibration made here is based on a case (River Arc) characterised by a high proportion of fine deposits and by the lithology of its catchment. Another location with a different proportion of fine deposits and different type of lithology could require a change in the weighting parameters, thus a new calibration may be needed for a different river.

3.2. Validation with the Wolman data

To validate the method, we compare the fine sediment areal ratio estimated from this new method with the Wolman data presented in Section 2.3.2. Indeed, since this method is totally independent from the previous one (close range photos analysed using *Basegrain*), bias should be limited in this validation step. Three bank-view photos before a dam flushing event and three after are selected to be analysed. Two Wolman patches were surveyed both before and after this flushing event and three (patches 3,4,5 in Figure 3) were surveyed after the flushing event. Results are presented in Figure 6, and details on statistical error determination for Wolman measurements are given in the Supplementary Material. Several interpretations can be made: (1) The spatial variation of the fine sediment deposits for different patches seems to be successfully reproduced by both methods. The average difference between Wolman and our method is 6% (except for Patch 4), which is in an acceptable range of uncertainty. However, a variation up to 5% between different photos for the same patch is noted (cf. Figure 6). This variation might be due to the variation of photo quality related to the weather condition (discussed in Section 3.4). (2) The Wolman method yields a relatively high bias of 25% for Patch 4 compared to the other patches. This high bias was due to the fact that the grain size distribution in Patch 4 is observed to be relatively extended and skewed towards the coarse end, which thus results in a statistical error for the estimation of D_5 corresponding to the fine sediment ($d < 4$ mm). It was reported by Rice and Church (1996) in the River Fraser and River Mamquam that the error on the estimation of D_5 class could be up to $\pm 30\%$ for a sample of 400 particles using the Wolman method. In addition, the image processing method could also have a bias for Patch 4. As Patch 4 was located far from the camera, the distortions during orthorectification are significantly higher than in near-field zones, which could explain the poorer results. The impact of position relative to the camera is discussed in Section 3.3.

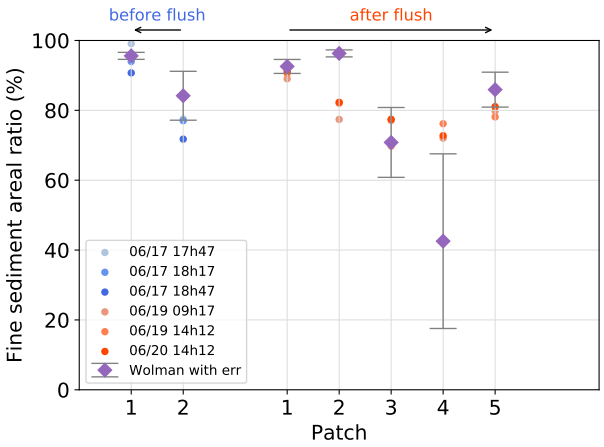

Figure 6: Comparison between the fine sediment class areal ratio $\Phi^f_{S,Wol}$ from the Wolman measurement and the fine sediment areal ratio $\Phi^f_{S,K}$ from the image processing method for the dam flushing event in 2019.

3.3. Uncertainties related to the orthorectification and image resolution

As shown in the validation results with the Wolman data, some discrepancies exist between the estimated fine sediment coverage and the field observation. Several sources of uncertainty from the orthorectification process could explain this bias. Two elements are investigated: the choice of the DEM and the influence of the oblique angle.

The DEM is a very important data within the orthorectification process, especially when the viewing angle largely differs from the vertical. In our case, the bar surface is very flat: elevation differences between the measured DEM and a flat DEM with a constant altitude are in a 50 cm range. The comparison between results obtained using orthoimages with a flat DEM and those with a measured one show that the overall bar emerged area is underestimated using the flat DEM by 3% compared to the measured DEM. The fine sediment deposits area is also underestimated with the flat DEM by 5.4% in average, this value being constant over time. The uncertainty due to the flat DEM is thus rather low, due to the small elevation differences to the flat surface, and the fact that the elevation variations are very smooth. Moreover, deposition and erosion processes that occurred during the studied time period did not yield thick deposits or erosions. Thus the bar altitude remained stable over time. However, if morphological evolutions of the bar surface were not negligible, or if a very high precision was required for area results, measured DEMs should replace the flat DEM during the orthorectification step, based on topographic surveys done a regular basis or after every hydrological event that might modify heights of the bar surface.

The viewing angle of the images could also be a major source of uncertainty. Since our images are taken from the left bank side with a highly oblique angle, local topographic details such as the presence of the coarse particles or vegetation could cause occlusions to the area behind these obstacles. To quantify this source of uncertainty, we compared the fine sediment coverage obtained from our orthorectified bank-view image with the result obtained from the drone image, which represents the real surface state of the bar. The selected bank-view image is taken on the very same day as the drone image. The fine sediment areas are 363.23 m^2 for the drone image subsampled at a 5 cm resolution (identical to the orthoimages resolution) and 370.12 m^2 for the orthoimage, which represents a difference below 2%, as shown in Figure 7.

We also tested the effect of image resolution on the fine sediment estimation. Specifically, we would like to know from which resolution, the quality of the results starts to degrade. Figure 7 shows the fine sediments areas obtained for each class of the clustering and for each subsampling resolution of the drone image compared to the bank orthoimage. The total fine area is given using the set of α_j^i determined in Section 3.1. Results obtained with varying resolutions are all very close to the average value 360.25 m^2, with a standard deviation of 6.88 m^2, except for the 15 cm and 20 cm resolutions, with a detected area of 283.26 m^2 and 265.17 m^2 respectively. Thus, results of the presented method are consistent and validated for a resolution range from 1 cm to 10 cm.

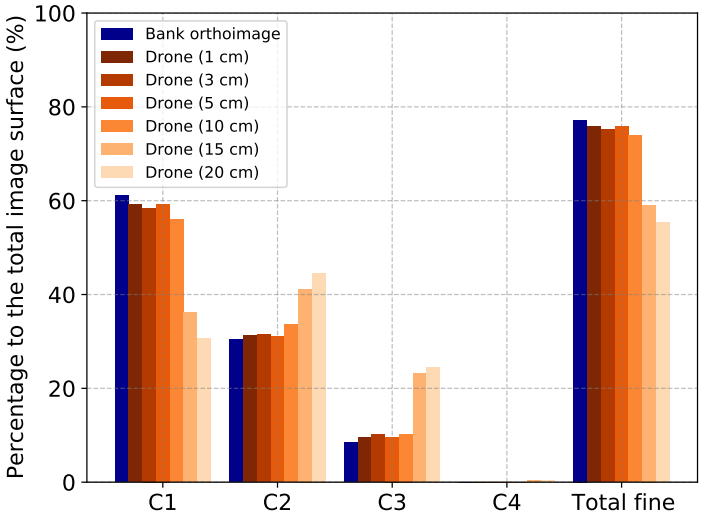

Figure 7: Effect of image resolutions on the fine sediment area estimation.

3.4. Effect of weather conditions on the image segmentation

Apart from the uncertainty due to the orthorectification process, the variation of the weather condition could also change the scene illumination and image quality (as shown in Table 1) and further impact the estimation of fine sediment deposits. It was thus investigated as described in section 2.7.

Results (see Figure 8a and Table 3) show that the new method is particularly robust, with a total standard variation of 2.7%. The robustness is especially evident for the images taken in the afternoon on sunny days with a 1.7% standard deviation, due to the fact that the edge of the coarse sediments can be clearly seen in the afternoon so that the limit between fine and coarse sediment becomes more distinct. In addition, the fine sediments under tree shadows can also be detected by the new method thanks to the HPF for removing the low frequency trend caused by the shadow.

Results for each image group are presented in Figure 8 and the mean and standard deviation are summarized in Table 3.

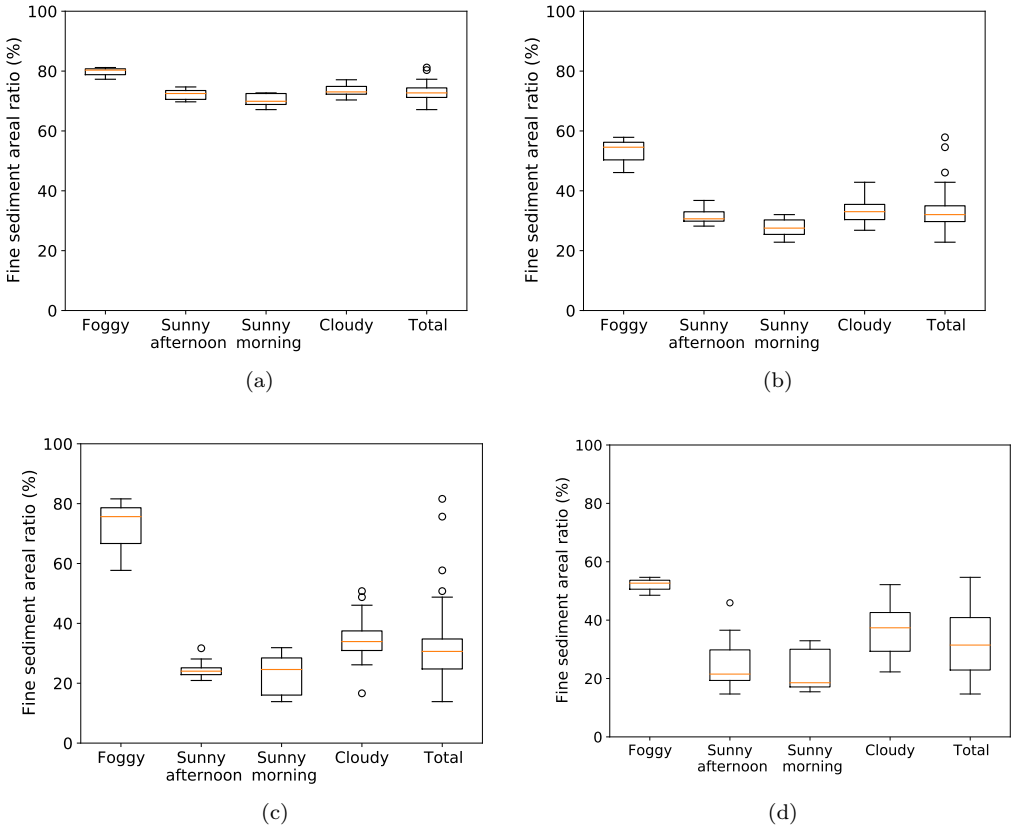

Figure 8: Detected of fine sediment areal ratio Φ_S^f under different weather conditions using (a) the present method, (b) the present method with a median filter, (c) the method of Camenen, and (d) the method of Carbonneau.

Method	Weather condition	Average Φ_S^f (%)	Standard deviation (%)
Present method	Foggy	79.6	1.6
	Sunny morning	70.4	2.0
	Sunny afternoon	72.1	1.7
	Cloudy	73.5	1.9
	Total	72.9	2.7
Present method with median filter	Foggy	52.8	5.0
	Sunny morning	27.7	3.1
	Sunny afternoon	31.6	2.6
	Cloudy	33.7	4.2
	Total	33.2	6.4
Method of Camenen	Foggy	71.7	12.4
	Sunny morning	22.9	6.8
	Sunny afternoon	24.5	3.0
	Cloudy	34.9	7.1
	Total	32.4	12.7
Method of Carbonneau	Foggy	52.0	3.1
	Sunny morning	22.5	7.1
	Sunny afternoon	25.1	9.3
	Cloudy	36.5	8.0
	Total	32.3	11.0

Table 3: Result of the variation of fine sediment areal ratio Φ_S^f due to the different weather condition for three methods

As shown in Figures 8 and 8a, results from the new method are significantly higher than results from other two methods from literature (Figures 8c and 8d). This may be due to the fact that the new method is calibrated with close-range photographs taken with a vertical angle. Inter-gravel fine particles are visible in these pictures, so the weighting parameters are calibrated accordingly. In contrast, to the authors' knowledge, both Camenen and Carbonneau methods were designed to detect main fine sediment patches excluding inter-gravel fine particle patches.

In order to confirm this hypothesis, a median filter is applied to our method. It aims at removing isolated pixels and narrow lines of pixels. The filter size is set to 5×5 pixels and it is applied to each class resulting from the K-means clustering. The weighting parameters are unchanged. As shown in

Figure 8b, the results of the present method with the median filter are similar to both Camenen and Carbonneau methods, with a total fine sediment ratio of 33.2% compared to 32.4% and 32.3% for Camenen's and Carbonneau's method, respectively. This confirms that the overall difference between the presented method (without the median filter) and both other methods is due to narrow lines of pixels or isolated pixels, corresponding to small inter-gravel fine sediment patches.

As shown in Figure 8, results for the foggy group are highly biased compared to the three other groups. A clear overestimation is observed compared to other groups (by approximately 30% for Camenen and Carbonneau methods). Indeed, the texture of the fine and coarse sediments on the bar surface cannot be clearly distinguished in the image because of the fog. If the present method (with or without the the median filter) is not as sensitive as the two other methods, there remains some bias. Consequently, the images taken in a foggy day should be discarded. Apart from the foggy weather, the new method appears to be the most robust to the different weather conditions compared to the other two methods. The robustness is particularly evident for the images taken on sunny days when cobble shadow can affect results. In addition, the fine sediments under the shadow of the tree can also be detected by the new method thanks to the HPF for removing the low frequency trend caused by the shadow. In contrast, fine sediments under shadows are often excluded by the other two methods, which explained a relatively low mean value (24.5% and 25.1% for the method of Camenen and Carbonneau, respectively) compared to our method value (31.6% with the median filter). Finally, the standard deviation of the new method for all 55 images is 6.4%, which is better than the method of Camenen (12.7%) and Carbonneau (11.0%).

All methods overestimated the deposit area when the fine sediments were completely dry. This could be due to the fact that the intensity of dry fine sediments and coarse sediments became similar. Some coarse sediment pixels could be classified into the fine sediment class leading to an overestimation of fine sediment coverage. We thus quantified the bias of this effect. The observed bias between the image with fully wet fine sediment deposits and the image with fully dry fine sediment deposits is 6.9%, 7.3%, and 17.0% for the proposed method, the method of Camenen, and the method of Carbonneau, respectively. Finally, the standard deviation of the new method for all 55 images is 2.7% (6.4% with the median filter), which is better than the method of Camenen (12.7%) and Carbonneau (11.0%). But if the foggy images are discarded, the Carbonneau method yields the larger dispersion. Also, the method of Camenen needs a calibration of the threshold of each class for each image, which makes it time-consuming when applying to a series of

images for continuously monitoring the fine sediment deposition on the bar surface.

Considering these limitations from both existing methods in the literature, we highlight the importance of applying the HPF after the 2D FFT on the images as it attenuates the effect of the varying brightness on the fine sediment segmentation. So the proposed method can easily be implemented to monitor the fine sediment deposits using a long image series with various conditions.

4. Conclusions

A new image processing methodology was developed in order to analyse the surface fine sediment deposits over gravel bars using images taken from the bank. This method combines a high-pass filter (performed in the Fourier domain) with a K-means clustering algorithm to automatically classify image pixels into K classes depending on the image intensity and texture. The fine sediment area is determined by applying weighting coefficients to the area of each class. A calibration of K and these weighting parameters α_K^i is conducted by optimising them with the ground truth fine sediment data acquired by 11 close range images with a 0.5 mm per pixel resolution. These images were processed using *Basegrain* software plus manual correction. The result of the calibration showed an optimised set of parameters when $K = 4$ with a minimum E_{RMS} of 5.5%. The method was validated with the Wolman pebble count method conducted on the bar surface. The fine sediment areal ratio from the new method was compared to the smallest class ($d < 4$ mm) of the grain size distribution obtained using the Wolman method. The average difference between the Wolman method and the new method are in an acceptable agreement having in mind uncertainties linked with both methodologies.

Given the possible variations caused by varying illumination (season, day time, sun/clouds, surface moisture), an assessment of the robustness of the new method was carried out. 55 images under four different weather conditions during a time period without notable hydrological events were selected to investigate the sensitivity of the method. The proposed method is found more robust compared to two methods from the literature: the method of Camenen (Camenen et al., 2013) based on the characteristics of local histogram and the method of Carbonneau based on the co-occurrence matrix value inspired by Carbonneau et al. (2005). However, the proposed method includes all patches of sediment including narrow inter-gravel patches, leading to much larger estimation of the deposit surface area compared to the two other methods. Using a median filter, the present method yields very

similar results as the two other methods, which corresponds to large patches of fine sediment deposits only.

Comparing the fine sediment detected from the orthorectified bank side image and from a drone image taken on the same day, a difference below 2% shows that the error caused by the orthorectification of the bank side image is negligible. In addition, we also checked the impact of different image resolutions on the new method. The new method produces consistent results for image resolutions ranging from 1 cm to 10 cm, which are typically resolutions of drone or bank images. However, it would be interesting to apply the method to different rivers, with different lithology. In the River Arc, black marlstone is prevailing. If the lithology is different, the calibration step should probably be undertaken again, to take the new sediment aspect into account. This would be a useful perspective to assert the applicability of the presented method to other catchments.

Finally, this new method could be used to monitor fine sediment deposits on gravel bars using a time series of images with resolution ranging from 1 to 10 cm since it is robust to varying illuminations. In the companion paper (in Part 2), we will detail links between the evolution of surface fine sediment deposits over this specific gravel bar on the River Arc and fine sediment transport drivers, such as water discharge, precipitation and wind, in order to obtain an insight of the fine sediment deposit dynamics over gravel bars in alpine rivers.

Acknowledgements

The authors thank INRAE and EDF (Electricité de France) for their support. This work was supported by the French National Research Agency (ANR) under the grant ANR-18-CE01-0020 (DEAR project) and Agence de l'Eau Rhône Méditerranée Corse under the grant Act°66 - AC IRSTEA. The study took place on an experimental site of the ZABR (Zone Atelier du Bassin Rhône) which is a CNRS-labelled site.

References

Antoine, G., Camenen, B., Jodeau, M., Némery, J., and Esteves, M. (2020). Downstream erosion and deposition dynamics of fine suspended sediments due to dam flushing. *Journal of Hydrology*, 585:124763.

Black, M., Carbonneau, P., Church, M., and Warburton, J. (2014). Mapping sub-pixel fluvial grain sizes with hyperspatial imagery. *Sedimentology*, 61(3):691–711.

Bradski, G. (2000). The OpenCV Library. *Dr. Dobb's Journal of Software Tools*.

Bunte, K. and Abt, S. R. (2001). Sampling surface and subsurface, particle-size distributions in wadable gravel- and cobble-bed streams for analyses in sediment transport, hydraulics, and streambed monitoring. General Technical Report RMRS-GTR-74, United State Department of Agriculture, Forest service, Rocky Mountain Research Station, Fort Collins, Colorado, USA. 430 p.

Buscombe, D. (2013). Transferable wavelet method for grain-size distribution from images of sediment surfaces and thin sections, and other natural granular patterns. *Sedimentology*, 60:1709–1732.

Buscombe, D. (2020). SediNet: a configurable deep learning model for mixed qualitative and quantitative optical granulometry. *Earth Surface Processes and Landforms*, 45(3).

Camenen, B., Herrero, A., Perret, E., Berni, C., Thollet, F., Buffet, A., Dramais, G., Le Bescond, C., and Lagouy, M. (2016). Estimation of the volume of a fine sediment deposit over a gravel bar during a flushing event. In *River Flow, Proc. 8th Int. Conf. on Fluvial Hydraulics*, page 8p., St Louis, Missouri, USA.

Camenen, B., Jodeau, M., and Jaballah, M. (2013). Estimate of fine sediment deposit dynamics over a gravel bar using photography analysis. *International Journal on Sediment Research*, 28(2):220–233.

Carbonneau, P. E., Bergeron, N. E., and Lane, S. N. (2004). Catchment-scale mapping of surface grain size in gravel bed rivers using airborne digital imagery. *Water Resources Research*, 40(W07202):1–11.

Carbonneau, P. E., Bergeron, N. E., and Lane, S. N. (2005). Texture-based image segmentation applied to the quantification of superficial sand in salmonid river gravels. *Earth Surface Processes & Landforms*, 30:121–127.

Carbonneau, P. E., Bizzi, S., and Marchetti, G. (2018). Robotic photosieving from low-cost multirotor sUAS: a proof-of-concept. *Earth Surface Processes and Landforms*, 43(5).

Cordier, F., Tassi, P., Claude, N., Crosato, A., Rodrigues, S., and Pham Van Bang, D. (2020). Bar pattern and sediment sorting in a channel contraction/expansion area: Application to the Loire River at Bréhémont (france). *Advances in Water Resources*, 140:103580.

694 Detert, M. and Weitbrecht, V. (2012). Automatic object detection to analyze
695 the geometry of gravel grains - a free stand-alone tool. *River Flow, Proc.*
696 *6th Int. Conf. on Fluvial Hydraulics*, 1:595–600.

697 Fausch, C. D., Torgersen, C. E., Baxter, C. V., and Li, H. W. (2002). Land-
698 scapes to riverscapes: Bridging the gap between research and conserva-
699 tion of stream fishes. *Bioscience*, 52:483–498.

700 Folk, R. and Ward, W. C. (1957). Brazos river bar : a study of significance
701 of grain size parameters. *Journal of Sediment Research*, 27:3–26.

702 Graham, D. J., Reid., I., and Rice, S. P. (2005). Automated sizing of coarse-
703 grained sediments: image-processing procedures. *Mathematical Geology*,
704 37:1–28.

705 Grams, P. E. and Schmidt, J. C. (2002). Streamflow regulation and multi-
706 level flood plain formation: Channel narrowing on the aggrading Green
707 River in the eastern Uinta Mountains, Colorado and Utah. *Geomorphol-*
708 *ogy*, 44:337–360.

709 Jaballah, M., Camenen, B., Paquier, A., and Jodeau, M. (2015). Alternate
710 bar development in an alpine river following engineering works. *Advances*
711 *in Water Resources*, 81:103–113.

712 Jain, A. K. and Dubes, R. C. (1988). *Algorithms for clustering data*. Prentice-
713 Hall, Inc.

714 Jain, A. K., Murty, M. N., and Flynn, P. J. (1999). Data clustering: A
715 review. *ACM Comput. Surv.*, 31(3):264–323.

716 Jodeau, M. (2007). *Morphodynamique d'un banc de galets en rivière*
717 *aménagée lors de crues [Gravel bar morphodynamics in an engineered*
718 *river during high flow events]*. PhD thesis, Claude Bernard University,
719 Lyon 1, , Cemagref Hydrology-Hydraulics Research Unit, Lyon, France.
720 205p. (in French).

721 Jourdain, C., Claude, N., Tassi, P., Cordier, F., and Antoine, G. (2020).
722 Morphodynamics of alternate bars in the presence of riparian vegetation.
723 *Earth Surface Processes & Landforms*, 45(5):1100–1122.

724 Juez, C., Hassan, M. and Franca, M. (2018) The origin of fine sediment de-
725 termines the observations of suspended sediment fluxes under unsteady
726 flow conditions. *Water Resources Research*, 54(8):5654–5669.

Kemp, P., Sear, D., Collins, A., Naden, P., and Jones, I. (2011). The impacts of fine sediment on riverine fish. *Hydrological Processes*, 25(11):1800–1821.

Kondolf, G. M. and Wilcock, P. R. (1996). The flushing flow problem: Defining and evaluating objectives. *Water Resources Research*, 32(8):2589–2599.

Konrad, C. P., Booth, D. B., Burges, S. J., and Montgomery, D. R. (2002). Partial entrainment of gravel bars during floods. *Water Resources Research*, 38(7):9–1–9–16.

Lambert, C. P. and Walling, D. E. (1988). Measurement of channel storage of suspended sediment in a gravel bed-river. *Catena*, 15:65–80.

Lang, N., Irniger, A., Rozniak, A., Hunziker, R., Wegner, J. D., and Schindler, K. (2020). GRAINet: Mapping grain size distributions in river beds from UAV images with convolutional neural networks. *Hydrology and Earth System Sciences Discussions*, pages 1–38.

Lenzi, M. A., Mao, L., and Comiti, F. (2003). Interannual variation of suspended sediment load and sediment yield in an alpine catchment. *Hydrological Sciences Journal*, 48(6):899–915.

Lisle, T. E. (1989). Sediment transport and resulting deposition in spawning gravels, north coastal California. *Water Resources Research*, 25(6):1303–1319.

Liu, J., Minami, S., Otsuki, H., Liu, B., and Ashida, K. (2004). Environmental impacts of coordinate sediment flushing. *Journal of Hydraulic Research*, 42(5):461–472.

MacQueen, J. et al. (1967). Some methods for classification and analysis of multivariate observations. In *Proceedings of the fifth Berkeley symposium on mathematical statistics and probability*, volume 1, pages 281–297. Oakland, CA, USA.

Misset, C., Recking, A., Legout, C., Valsangkar, N., Bodereau, N., Zanker, S., Poirel, A., and Borgniet, L. (2019). The dynamics of suspended sediment in a typical alpine alluvial river reach: Insight from a seasonal survey. *Water Resources Research*, 55(12):10918–10934.

Misset, C., Recking, A., Legout, C., Viana-Bandeira, B., and Poirel, A. (2021). Assessment of fine sediment river bed stocks in seven Alpine catchments. *CATENA*, 196:104916.

762 Navratil, O., Legout, C., Gateuille, D., Esteves, M., and Liébault, F. (2010).
763 Assessment of intermediate fine sediment storage in a braided river reach
764 (southern french prealps). *Hydrological Processes*, 24:1318–1332.

765 Nelson, P. A., Bellugi, D., and Dietrich, W. E. (2014). Delineation of river
766 bed-surface patches by clustering high-resolution spatial grain size data.
767 *Geomorphology*, 205:102–119. Discontinuities in Fluvial Systems.

768 Otsu, N. (1979). A threshold selection method from gray-level histograms.
769 *IEEE Transactions on Systems, Man, and Cybernetics*, 9(1):62–66.

770 Pagano, S. G., Rainato, R., García-Rama, A., Gentile, F., and Lenzi, M. A.
771 (2019). Analysis of suspended sediment dynamics at event scale: com-
772 parison between a Mediterranean and an Alpine basin. *Hydrological*
773 *Sciences Journal*, 64(8):948–961.

774 Piqué, G., López-Tarazón, J. A., and Batalla, R. J. (2014). Variability of
775 in-channel sediment storage in a river draining highly erodible areas (the
776 Isábena, Ebro Basin). *Journal of Soils and Sediments*, 14(12):2031–2044.

777 Purinton, B. and Bookhagen, B. (2019). Introducing PebbleCounts: a grain-
778 sizing tool for photo surveys of dynamic gravel-bed rivers. *Earth Surface*
779 *Dynamics*, 7(3):859–877. Publisher: Copernicus GmbH.

780 Rathburn, S. and Wohl, E. (2003). Predicting fine sediment dynamics along
781 a pool riffle mountain channel. *Geomorphology*, 55:111–124.

782 Rice, S. and Church, M. (1996). Sampling surficial fluvial gravels; the pre-
783 cision of size distribution percentile sediments. *Journal of Sedimentary*
784 *Research*, 66(3):654–665. Publisher: GeoScienceWorld.

785 Rubin, J., Glimsater, C., and Jarvi, T. (2004). Characteristics and rehabili-
786 tation of the spawning habitats of the sea trout, Salmotrutta, in Gotland
787 (Sweden). *Fisheries Management and Ecology*, 11:15–22.

788 Vercruysse, K., Grabowski, R. C., and Rickson, R. J. (2017). Suspended
789 sediment transport dynamics in rivers: Multi-scale drivers of temporal
790 variation. *Earth-Science Reviews*, 166:38–52.

791 Verdú, J. M., Batalla, R. J., and Martínez-Casasnovas, J. A. (2005). High-
792 resolution grain-size characterisation of gravelbars usingimagery analysis
793 and geo-statistics. *Geomorphology*, 72(1-4):73–93.

794 Wang, Y.-H., Wang, Y.-H., and Tang, L.-Q. (2008). On the formation
795 of couplet-style stratifications. *International Journal on Sediment Re-*
796 *search*, 23:85–91.

797 Wohl, E. E. and Cenderelli, D. A. (2000). Sediment deposition and trans-
798 port patterns following a reservoir sediment release. *Water Resources*
799 *Research*, 36(1):319–333.

800 Wood, P. J. and Armitage, P. D. (1997). Biological effects of fine sediment
801 in the lotic environment. *Environmental Management*, 21:203–217.

Fine sediment dynamics over a gravel bar. Part 1: Validation of a image-base segmentation

Junjian Deng, Lionel Pénard, Thomas Drevet, Benoît Camenen

1

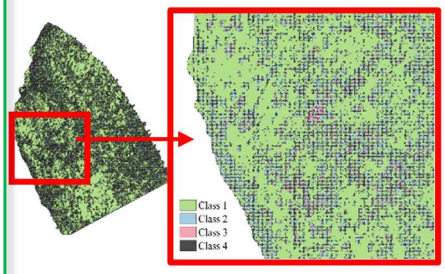

$$\phi^f_{S,K} = \frac{\sum_{i=1}^{K} \alpha_K^i S_K^i}{S_{image}}$$

2

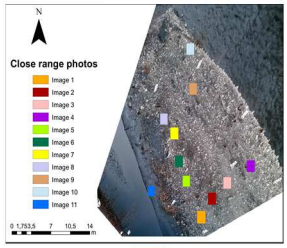

$$\phi^f_{S,Base} = 1 - \frac{S_{detected}}{S_{image}}$$

3

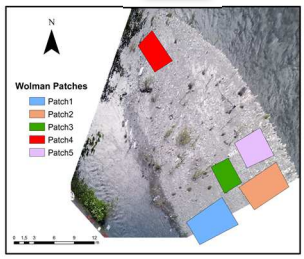

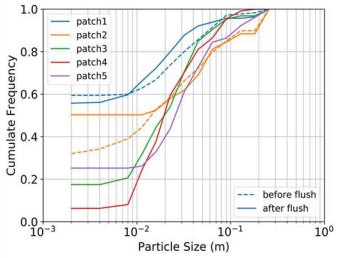

$$\phi^f_{S,Wol} = \frac{\phi^f_{V,Wol}}{D^f_{Wol} S^f_{Wol}}$$

4

Calibration with ground truth data

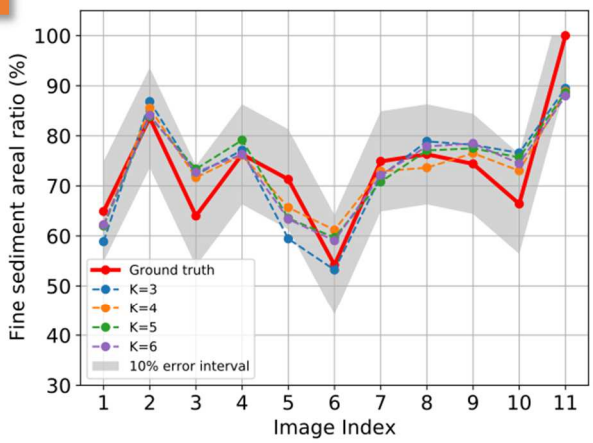

$$\phi^f_{S,K} = \frac{1.0 \times S^1_{K=4} + 0.5 \times S^2_{K=4} + 0.1 \times S^3_{K=4} + 0.0 \times S^4_{K=4}}{S_{image}}$$

5

Validation with in-situ measurement

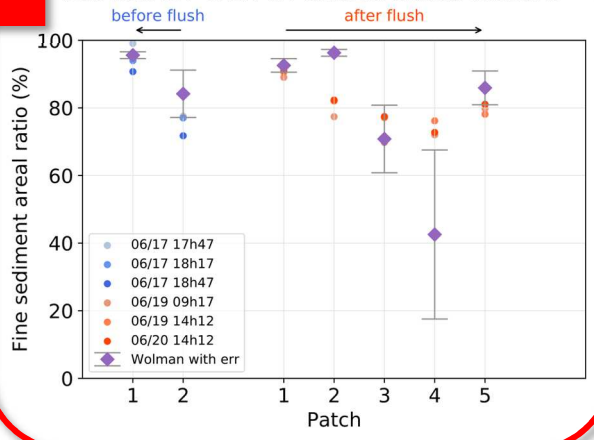

1. Image-base segmentation methodology → Uncalibrated fine sediment areal ratio
2. BASEGRAIN + manual correction → Ground truth data of fine sediment coverage
3. In-situ measurement of grain size distribution (Wolman pebble count) → Field fine sediment proportion
4. Calibration with ground truth data → Calibrated fine sediment areal ratio
5. Validation with in-situ measurement → Validation of new methodology